


Buoyancy-Induced Convection Driven by Frontal PolymerizationY. Gao^{1,2}, J. E. Paul^{1,3}, M. Chen^{1,2}, L. Hong⁴, L. P. Chamorro⁴, N. R. Sottos^{1,3,*} and P. H. Geubelle^{1,2,†}¹*Beckman Institute for Advanced Science and Technology, University of Illinois, Urbana, Illinois 61801, USA*²*Department of Aerospace Engineering, University of Illinois, Urbana, Illinois 61801, USA*³*Department of Material Science and Engineering, University of Illinois, Urbana, Illinois 61801, USA*⁴*Department of Mechanical Science and Engineering, University of Illinois, Urbana, Illinois 61801, USA* (Received 28 June 2022; revised 17 October 2022; accepted 5 December 2022; published 9 January 2023)

In this Letter, we study the interaction between a self-sustaining exothermic reaction front propagating in a direction perpendicular to that of gravity and the buoyancy-driven convective flow during frontal polymerization (FP) of a low-viscosity monomer resin. As the polymerization front transforms the liquid monomer into the solid polymer, the large thermal gradients associated with the propagating front sustain a natural convection of the fluid ahead of the front. The fluid convection in turn affects the reaction-diffusion (RD) dynamics and the shape of the front. Detailed multiphysics numerical analyses and particle image velocimetry experiments reveal this coupling between natural convection and frontal polymerization. The frontal Rayleigh (Ra) number affects the magnitude of the velocity field and the inclination of the front. A higher Ra number drives instability during FP, leading to the observation of thermal-chemical patterns with tunable wavelengths and magnitudes.

DOI: [10.1103/PhysRevLett.130.028101](https://doi.org/10.1103/PhysRevLett.130.028101)

The interaction between the reaction-diffusion (RD) dynamics and associated fluid motions of an autocatalytic reaction front has received considerable research attention [1–5]. The variation in physical parameters at the boundary [6] or in the bulk region of the system [7] can lead to fluid convection. The reaction-induced hydrodynamic flows can couple back, influencing the front velocity and shape [8–11]. Moreover, the reaction-diffusion-convection (RDC) dynamics can drive chemical oscillations [12,13], which are integral to broad applications such as quorum sensing [14], chemical artificial intelligence [15], and stimuli-responsive materials [16].

Frontal polymerization (FP) involves a self-propagating chemical front that transforms the monomer into a polymer [17–23] and has been reported as a fast, efficient manufacturing technique for functional polymeric materials [24–26]. Although FP is usually considered a reaction-diffusion process for polymeric systems, previous experiments [27,28] and mathematical analyses [29,30] report that buoyancy-induced convection can change the front velocity and induce instabilities when the front propagates parallel (descending) or against the gravitation (ascending), as convection across the front transfers fresh reactants closer or further to the reaction site [28,31]. In this Letter, we report a combined numerical and experimental study of the interactions between the polymerization front propagating in a direction perpendicular to gravity and the buoyancy-driven convective flow in the FP of dicyclopentadiene (DCPD). Different from other autocatalytic systems that generate liquid products [32–34], the significant increase in the viscosity of polymeric products [35] limits the convection

to a narrower region ahead of the reaction site. The convection parallel to the polymerization front is quantitatively characterized and revealed to induce pattern-forming instabilities overlooked by the reaction-diffusion theory that does not account for natural convection. This Letter enables the potential for fabricating polymeric materials with controllable patterns and heterogeneous properties [36] in closed mold systems.

On the numerical side, we capture the fluid convection effects on FP by combining the reaction-diffusion partial differential equations with the incompressible Navier-Stokes equations under the Boussinesq approximation as [37]

$$\begin{aligned} \rho C_p \left(\frac{\partial T}{\partial t} + \mathbf{u} \cdot \nabla T \right) &= \kappa \nabla^2 T + \rho H_r \left(\frac{\partial \alpha}{\partial t} + \mathbf{u} \cdot \nabla \alpha \right), \\ \frac{\partial \alpha}{\partial t} + \mathbf{u} \cdot \nabla \alpha &= A \exp \left(-\frac{E}{RT} \right) f(\alpha), \\ \nabla \cdot \mathbf{u} &= 0, \\ \frac{\partial \mathbf{u}}{\partial t} + \mathbf{u} \cdot \nabla \mathbf{u} &= -\frac{1}{\rho} \nabla P + \nabla \cdot [\nu (\nabla \mathbf{u} + (\nabla \mathbf{u})^T)] + \mathbf{F}. \end{aligned} \quad (1)$$

In this 2D study, the four dependent variables are the temperature $T(x, y, t)$, degree of cure $\alpha(x, y, t)$, pressure $P(x, y, t)$, and velocity vector $\mathbf{u} = [u_x(x, y, t), u_y(x, y, t)]$, with (x, y) and t denoting the spatial coordinates and time, respectively. The degree of cure α takes values between 0 (monomer) and 1 (polymer) and describes the fractional conversion based on the enthalpy of the reaction. In the first

relationship, κ , C_p , ρ , and H_r denote the thermal conductivity, heat capacity, density, and heat of reaction of the resin, respectively. The second relationship corresponds to the cure kinetics model approximated with the n th-order model $f(\alpha) = (1 - \alpha)^n$, while A , E , and $R(= 8.314 \text{ J/kg K})$ represent the preexponential factor, the activation energy, and the ideal gas constant, respectively. The approximation yields front velocity and temperature values close to experimental measurements [38]. The molecular diffusion is neglected in the model.

The third relation prescribes the mass conservation, while the fourth equation corresponds to the conservation of momentum, with ν denoting the kinematic viscosity. The body force term describes the fluid flow driven by the temperature change $\mathbf{F} = -\rho\beta\mathbf{g}\Delta T$, where β , \mathbf{g} , and ΔT are the thermal expansion coefficient of the resin, gravitational acceleration vector ($0, -9.81 \text{ m/s}^2$), and the temperature change.

The governing equations (1) are solved over a rectangular numerical domain of length $l = 40 \text{ mm}$ (in the x direction) and height $h = 4 \text{ mm}$ (in the y direction) with the following initial and boundary conditions:

$$\begin{aligned} T(x, y, 0) &= T_0, 0 \leq x \leq l, 0 \leq y \leq h, \\ \alpha(x, y, 0) &= \alpha_0, 0 \leq x \leq l, 0 \leq y \leq h, \\ T(0, y, t) &= T_{\text{trig}}, 0 \leq y \leq h, 0 \leq t \leq t_{\text{trig}}, \\ \frac{\partial T}{\partial x}(0, y, t) &= 0, 0 \leq y \leq h, t > t_{\text{trig}}, \end{aligned} \quad (2)$$

where T_0 (20°C), α_0 (10^{-5}), T_{trig} (200°C), and t_{trig} (1 s) are the initial temperature and degree of cure, triggering temperature, and triggering time, respectively. Adiabatic boundary conditions are applied along all other boundaries. No-slip boundary conditions are applied along all boundaries.

The Multiphysics Object-Oriented Simulation Environment (MOOSE) [39], an open source C++ finite element solver that includes robust mesh and time-step adaptivity, is adopted in this study to capture the sharp gradients in temperature, degree of cure, and velocity in the vicinity of the advancing polymerization front. See Tables S1 and S2 in the Supplemental Material [40] for material properties and cure kinetics parameters.

Figures 1(a) and 1(b) display snapshots of the distributions of degree of cure α and normalized temperature $T^* = (T - T_0)/[H_r(1 - \alpha_0)/C_p]$, respectively, with the blue arrow denoting the direction of front propagation. In the vicinity of the front, the reaction heat leads to a sharp thermal gradient and gives rise to a clockwise vortex visualized by the velocity vector field ahead of the front. As α increases from 0 to 1, the viscosity grows by ~ 6 orders of magnitude (Fig. S1 of Supplemental Material [40]), thereby zeroing the velocity field behind the front. As the vortex moves with the front, the associated convective flow transfers some of the reaction heat to the positive y

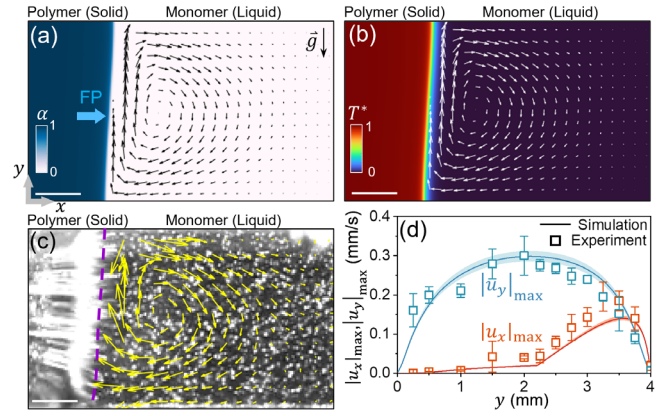


FIG. 1. Numerical snapshots of degree of cure α (a) and normalized temperature T^* (b) when the front has reached a steady state. (c) Side-view optical image of FP experiment in a closed mold 20 s after initiation. The arrows in (a)–(c) denote the direction of local velocity vector \mathbf{u} . All scale bars denote 1 mm. (d) Simulated and experimental maximum values of fluid velocity components at different vertical locations y .

direction, leading to an inclined front. After some initial transients associated with the front ignition along the left edge of the domain, the front reaches a steady-state velocity $v_f = 1.30 \text{ mm/s}$ and an inclination angle θ_f of 2.40° . This steady-state velocity is greater than that predicted by the reaction-diffusion relations in the absence of convection (1.23 mm/s) (Fig. S2 of Supplemental Material [40]), indicating that the buoyancy-driven convection facilitates the front propagation.

FP experiments were performed in a rectangular closed glass mold with dimensions of 7.5 cm (in the FP direction) $\times 2.5 \text{ cm} \times 0.4 \text{ cm}$ to validate the numerical results. Silver hollow spheres were added to the DCPD resin to perform particle image velocimetry (PIV) during frontal polymerization in a closed mold system. More experimental details are included in the Supplemental Material [40].

Figure 1(c) is a representative side-view optical image of an experiment conducted at room temperature $\sim 20^\circ\text{C}$ and without preheating the resin ($\alpha_0 \sim 0$), consistent with the numerical settings in Figs. 1(a) and 1(b). The dashed line indicates the location of the front. Extracted by PIV, the velocity field ahead of the front \mathbf{u} shows a clockwise vortex consistent with the numerical analyses. Figure 1(d) presents the y variation of the simulated and measured maximum velocity vector components $|u_x|_{\text{max}}$ and $|u_y|_{\text{max}}$, showing a good agreement. As expected, the walls of the glass mold at $y = 0$ and 4 mm (no-slip boundary conditions in the simulation) enforce zero $|u_x|_{\text{max}}$ and $|u_y|_{\text{max}}$.

A detailed numerical parametric study reveals that both the front inclination angle and the maximum fluid velocity magnitude decrease nonlinearly with the initial temperature T_0 and degree of cure α_0 (Fig. S3 in the Supplemental Material [40]). To better characterize the dependence of the solution on the key parameters that define the

reaction-diffusion-convection problem, we rewrite Eq. (1) in its nondimensional form as

$$\begin{aligned} \frac{\partial T^*}{\partial t^*} + \mathbf{u}^* \cdot \nabla T^* &= \nabla^2 T^* + \frac{\partial \alpha}{\partial t^*} + \mathbf{u}^* \cdot \nabla \alpha, \\ \frac{\partial \alpha}{\partial t^*} + \mathbf{u}^* \cdot \nabla \alpha &= Z \exp \left[\frac{\delta(T^* - 1)}{T^* + \eta} \right] f(\alpha), \\ \nabla \cdot \mathbf{u}^* &= 0, \\ \frac{\partial \mathbf{u}^*}{\partial t^*} + \mathbf{u}^* \cdot \nabla \mathbf{u}^* &= -\nabla P^* + \nabla \cdot [\text{Pr}(\nabla \mathbf{u}^* + (\nabla \mathbf{u}^*)^T)] \\ &\quad - \text{Pr Ra} T^* \hat{\mathbf{g}}, \end{aligned} \quad (3)$$

where superscripts “*” indicate variables reduced with the characteristic time $t_c = D/v_c^2$, length $l_c = D/v_c$, pressure $P_c = v_c^2 \rho$, and velocity $v_c = [(A\kappa RT_f^2/\rho H_r(1-\alpha_0)E) \exp(-E/RT_f)]^{0.5}$. $T_f = T_0 + H_r(1-\alpha_0)/C_p$ is the adiabatic front temperature, $D = \kappa/(\rho C_p)$ is the thermal diffusivity of the resin, and the unit vector $\hat{\mathbf{g}}$ denotes the direction of gravity. The characteristic velocity v_c is proportional to the steady-state front velocity v_f [41]. In the second equation, $Z = H_r(1-\alpha_0)E/(C_p RT_f^2)$ is the Zeldovich number, while the nondimensional parameters δ and η are defined as $\delta = E/(RT_f)$ and $\eta = T_0 C_p/[H_r(1-\alpha_0)]$. In (3)₄, $\text{Pr} = \nu/D$ is the Prandtl number, and $\text{Ra} = \beta |g| H_r(1-\alpha_0) D^2 / (C_p \nu v_c^3)$ is the frontal Rayleigh number that quantifies the buoyancy effect and is used hereafter to characterize the FP-driven fluid convection. Considering the dependence of ν on α , Ra is evaluated with the viscosity value corresponding to $\alpha = \alpha_0$.

As shown in Fig. 2, the numerically predicted normalized fluid velocity magnitude $|\mathbf{u}|_{\max}/v_c$ (cool-color circles) increases linearly with Ra. All results were taken within the steady-state regime, with the uncertainty (error bars) resulting from averaging data in ~ 200 simulation frames in each case. A stronger fluid momentum produces a larger inclination angle θ_f (warm-color circles), which also

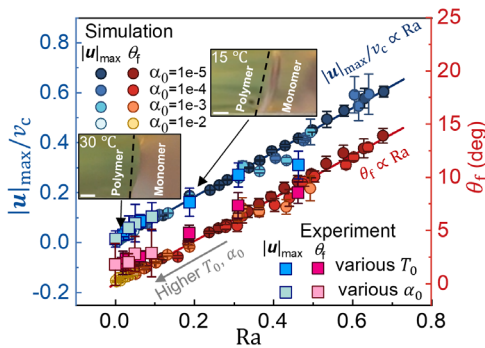


FIG. 2. Numerical (circles) and experimental (squares) results of the normalized maximum fluid velocity magnitude $|\mathbf{u}|_{\max}/v_c$ and inclination angle θ_f as functions of the frontal Rayleigh number Ra, where v_c is a characteristic velocity. Optical experimental images are shown in insets with scale bars representing 1 mm.

depends linearly on Ra. For all numerical data presented in Fig. 2, T_0 is chosen between 0 and 35 °C, which is typical for the processing temperature of FP [42,43]. As the initial temperature increases (i.e., as Ra decreases), the front speed v_f increases and the solid polymer forms more rapidly right at the location with the buoyancy effect, limiting the fluid convection. Similarly, as α_0 is increased by pregelling the resin before FP, the associated increase in ν leads to lower values of Ra for a fixed T_0 value. With a lower Ra, the effect of fluid convection on the front propagation is reduced, and the RDC and RD models converge (Fig. S2 in the Supplemental Material [40]).

Two sets of FP experiments were conducted at multiple T_0 values between 5 and 35 °C without precure (i.e., $\alpha_0 \sim 0$) and for α_0 values ranging between ~ 0 and 0.037 at room temperature (20 °C). The averaged steady-state values and errors of $|\mathbf{u}|_{\max}$ and θ_f obtained from 40 frames around $t = 20$ s in each experiment video are presented in Fig. 2 as square symbols and show good agreement with the numerical results. Two insets depict optical images of the steady-state front in experiments conducted at $T_0 = 15$ and 30 °C, with the liquid monomer and solid polymer shown in dark pink (right) and yellow (left) colors, respectively. The curved shape of the front in experiments was caused by the heat loss to the glass mold [44], which does not influence $|\mathbf{u}|_{\max}/v_c$ or θ_f , as demonstrated in Fig. S4 in the Supplemental Material [40].

As shown in Video S1 available in the Supplemental Material [40], the front experiences instabilities at $T_0 = 10$ °C. These instabilities are captured numerically in Fig. 3(a), which presents two numerical snapshots of the T^* distributions obtained for $T_0 = 10$ °C and $\alpha_0 = 10^{-5}$. These results indicate the presence of multihead spin-mode instabilities, where thermal heads (i.e., local regions of high temperature) are observed to separate and merge with each other, as indicated by the white arrows. When the thermal heads reach the top and bottom boundaries of the domain, they bounce back and keep interacting with the adjacent heads. The front shape in this “quasi-steady-state regime” thus switches back and forth between the two states separated by ~ 0.17 s, leading to periodic reaction patterns with tunable, temperature-dependent features shown in Fig. 3(b).

At $T_0 = 15$ °C (I), no reaction patterns are observed and the front propagation is stable. As T_0 decreases to 10 (II) and 5 °C (III), wavelike reaction patterns emerge containing regions of high reaction rate (lighted regions in the figure) separated by (darker) bands of low reaction rates. The motion of the thermal heads is highlighted by the white arrows. The magnitude of maximum reaction rates $\dot{\alpha}_{\max}$ is higher at a lower T_0 , indicating higher instantaneous temperatures and a higher instability for the front [42]. The wavelength of the pattern also increases with decreasing T_0 . In addition, the average distance between the location of thermal heads increases, characterized by the pattern

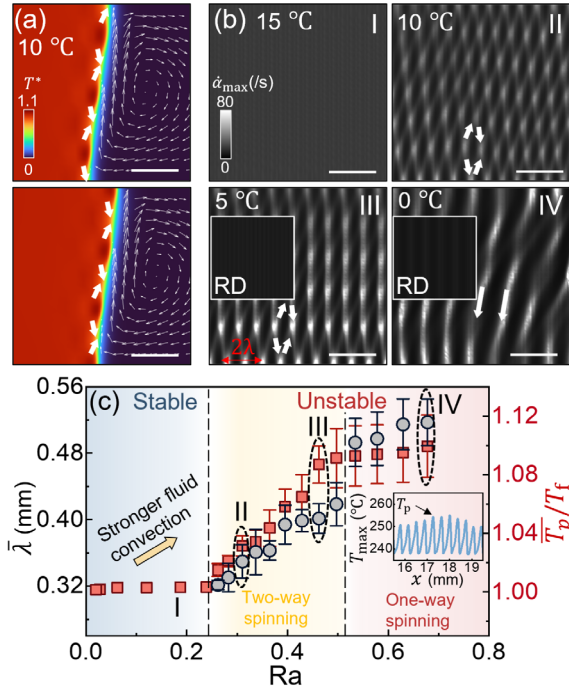


FIG. 3. (a) Multihead spin-mode instabilities observed in simulations. (b) Spatial variations of the maximum reaction rate $\dot{\alpha}_{\max}$ with different T_0 values, where λ denotes the wavelength of patterns. All scale bars represent 1 mm. Reaction patterns are not observed with the reaction-diffusion theory (insets). (c) Average wavelength $\bar{\lambda}$ and average temperature ratio \bar{T}_p/T_f as functions of Rayleigh number Ra , where T_p is the instability peak temperature observed at the bottom boundary (inset).

wavelength λ along the bottom boundary of the system (marked by the red arrow). With a further reduced $T_0 = 0^\circ\text{C}$, the reaction pattern is featured by inclined serpentine lines with local high intensities that correspond to thermal heads. Unlike II and III, the connections between dots in the horizontal direction vanish, suggesting a different propagating regime: thermal heads spin to the negative y direction instead of separating in two directions (white arrows, Video. S2 in the Supplemental Material [40]). The instability-driven patterns are not observed with the RD theory.

Based on the observed propagating regimes presented in Figs. 3(b), and 3(c) presents the Ra dependence of the characteristic pattern features, i.e., the average wavelength $\bar{\lambda}$ and instability temperature ratio \bar{T}_p/T_f , where T_p is the temperature at the instability peak observed at the bottom boundary (inset). With a Ra smaller than 0.24 ($T_0 > 12.5^\circ\text{C}$), the limited momentum of the fluid convection is insufficient to disturb the stable front propagation. In these cases, for which Fig. 3(b)-I serves as an illustrative example, $\bar{T}_p/T_f = 1$ and no instability or patterns are observed.

When Ra is between 0.24 and 0.37, the stronger fluid convection leads to larger inclination angles (Fig. 2) and heat exchange parallel to the front, which impacts the

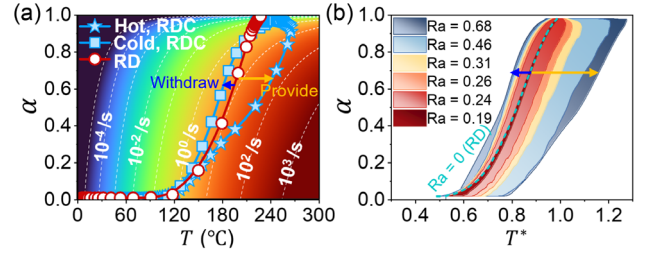


FIG. 4. (a) Reaction rate $\dot{\alpha}$ (color, in logarithmic scale) as a function of the temperature T and degree of cure α . Evolution of typical $\alpha - T^*$ relationships in a patterning reaction-diffusion-convection system (squares and stars) and a pattern-free reaction-diffusion system (circles). (b) Spectrum of $\alpha - T^*$ relationships in reaction-diffusion-convection systems with various frontal Rayleigh number Ra . The dashed curve denotes the reaction-diffusion system ($Ra = 0$).

reaction-diffusion power balance [36]. Consequently, multihead two-way spinning instabilities occur along with the inclined front profile (unstable region), exemplified by Figs. 3(a) and 3(b)-II, III. The thermal peaks result in \bar{T}_p/T_f values > 1 , which increases with Ra . With $Ra > 0.5$ ($T_0 < 4.5^\circ\text{C}$), the thermal front is less active so that the spin in the positive y direction along with the front profile is eliminated by the fluid, leading to a one-way spin mode [Fig. 3(b)-IV]. The transition in the propagating regime leads to a jump in $\bar{\lambda}$ while the increase in \bar{T}_p/T_f with Ra is no longer significant.

To elaborate on the correlation between the convection and FP, Fig. 4(a) presents the reaction rate $\dot{\alpha}$ with a logarithmic color scale given specific values of temperature T and α . Meanwhile, the evolution of the α and T at the locations with high (stars, hot) and low (squares, cold) reaction rates in a patterning FP system [$T_0 = 5^\circ\text{C}$, $\alpha_0 = 10^{-5}$, Fig. 3(b)-III] is displayed, and the $\alpha - T$ curve under the same condition but without convection effects (red circles, pattern-free) is also shown as a reference. The discrepancy between RDC and RD systems indicates that the convection transfers part of the reaction heat from cold (“withdraw,” blue arrow) to hot (“provide,” yellow arrow) regions within the front, leading to variations in local temperatures. Consequently, the disturbed temperature distribution leads to heterogeneous reaction rates and drives the formation of reaction patterns. Figure 4(b) compares the range of $\alpha - T^*$ values in RDC systems with various Ra numbers. At a higher Ra , the fluid momentum is enhanced, disturbing the reaction to a larger extent, which results in a wider $\alpha - T^*$ range. In addition, the intensity of the reaction pattern is amplified as a higher maximum reaction rate can be achieved. Reducing Ra restricts the convection, and the $\alpha - T^*$ evolution converges to that in a RD system ($Ra = 0$).

To summarize, we have presented the interaction between a self-propagating polymerization front and the associated buoyant convection during the frontal polymerization of

dicyclopentadiene. The reaction heat drives a fluid vortex ahead of the front, which leads to inclined front shapes. The frontal Rayleigh number, which compares the effects of the buoyant flow and of the frontal polymerization, governs both the maximum fluid velocity and front inclination angle with linear relationships, confirmed with both simulations and experiments. Moreover, strong fluid momentum can introduce heat exchange parallel to the front, which disturbs the stable front propagation and leads to multihead spin-mode instabilities. The emergence of different instability regimes, from stable to one-way and two-way spin modes, and the characteristic features of wavelength and instability peak temperature, also depend on the value of Ra. The interaction and patterning mechanisms provide a fundamental understanding of frontal polymerization beyond the scope of reaction-diffusion dynamics and are helpful for manufacturing polymeric parts with tunable heterogeneous features at the submillimeter level.

This work was supported by the U.S. Air Force Office of Scientific Research through Award FA9550-20-1-0194 as part of the Center of Excellence in Self-healing and Morphogenic Manufacturing. The authors also acknowledge the support of the National Science Foundation for Grant No. 1933932 through the GOALI: Manufacturing USA: Energy Efficient Processing of Thermosetting Polymers and Composites.

Y. G. and J. E. P. contributed equally to this work.

*Corresponding author.

n-sottos@illinois.edu

†Corresponding author.

geubelle@illinois.edu

- [1] M. J. Hauser and R. H. Simoyi, *Phys. Lett. A* **191**, 31 (1994).
- [2] D. A. Vasquez, J. M. Little, J. W. Wilder, and B. F. Edwards, *Phys. Rev. E* **50**, 280 (1994).
- [3] H. Kitahata, R. Aihara, N. Magome, and K. Yoshikawa, *J. Chem. Phys.* **116**, 5666 (2002).
- [4] I. Nagypal, G. Bazsa, and I. R. Epstein, *J. Am. Chem. Soc.* **108**, 3635 (1986).
- [5] J. A. Pojman and I. R. Epstein, *J. Phys. Chem.* **94**, 4966 (1990).
- [6] P. Bába, L. Rongy, A. De Wit, M. J. B. Hauser, Á. Tóth, and D. Horváth, *Phys. Rev. Lett.* **121**, 024501 (2018).
- [7] G. Schusztter, T. Tóth, D. Horváth, and Á. Tóth, *Phys. Rev. E* **79**, 016216 (2009).
- [8] A. De Wit, *Phys. Rev. Lett.* **87**, 054502 (2001).
- [9] I. B. Malham, N. Jarrige, J. Martin, N. Rakotomalala, L. Talon, and D. Salin, *J. Chem. Phys.* **133**, 244505 (2010).
- [10] L. Rongy, G. Schusztter, Z. Sinkó, T. Tóth, D. Horváth, A. Tóth, and A. De Wit, *Chaos* **19**, 023110 (2009).
- [11] J. A. Pojman, I. R. Epstein, T. J. McManus, and K. Showalter, *J. Phys. Chem.* **95**, 1299 (1991).
- [12] M. A. Budroni, V. Upadhyay, and L. Rongy, *Phys. Rev. Lett.* **122**, 244502 (2019).
- [13] L. Rongy, A. De Wit, and G. Homsy, *Phys. Fluids* **20**, 072103 (2008).
- [14] A. F. Taylor, M. R. Tinsley, F. Wang, Z. Huang, and K. Showalter, *Science* **323**, 614 (2009).
- [15] K. Gizynski and J. Gorecki, *Phys. Chem. Chem. Phys.* **19**, 28808 (2017).
- [16] R. Yoshida, *Adv. Mater.* **22**, 3463 (2010).
- [17] N. M. Chechilo, R. J. Khvilivitskii, and N. S. Enikolopyan, *Dokl. Akad. Nauk SSSR* **204**, 1180 (1972).
- [18] J. A. Pojman, V. M. Ilyashenko, and A. M. Khan, *J. Chem. Soc., Faraday Trans.* **92**, 2825 (1996).
- [19] S. Chen, Y. Tian, L. Chen, and T. Hu, *Chem. Mater.* **18**, 2159 (2006).
- [20] C. Nason, T. Roper, C. Hoyle, and J. A. Pojman, *Macromolecules* **38**, 5506 (2005).
- [21] A. Ruiiu, D. Sanna, V. Alzari, D. Nuvoli, and A. Mariani, *J. Polym. Sci., A-2, Polym. Phys.* **52**, 2776 (2014).
- [22] D. Nuvoli, V. Alzari, J. A. Pojman, V. Sanna, A. Ruiiu, D. Sanna, G. Malucelli, and A. Mariani, *ACS Appl. Mater. Interfaces* **7**, 3600 (2015).
- [23] M. Sangermano, A. D'Anna, C. Marro, N. Klikovits, and R. Liska, *Composites Part B* **143**, 168 (2018).
- [24] I. D. Robertson, M. Yourdkhani, P. J. Centellas, J. E. Aw, D. G. Ivanoff, E. Goli, E. M. Lloyd, L. M. Dean, N. R. Sottos, P. H. Geubelle *et al.*, *Nature (London)* **557**, 223 (2018).
- [25] K. Bansal, J. A. Pojman, D. Webster, and M. Quadir, *ACS Macro Lett.* **9**, 169 (2020).
- [26] C. Yu, C.-F. Wang, and S. Chen, *Adv. Funct. Mater.* **24**, 1235 (2014).
- [27] J. A. Pojman, R. Craven, A. Khan, and W. West, *J. Phys. Chem.* **96**, 7466 (1992).
- [28] B. McCaughey, J. A. Pojman, C. Simmons, and V. Volpert, *Chaos* **8**, 520 (1998).
- [29] M. Garbey, A. Taik, and V. Volpert, *Q. Appl. Math.* **56**, 1 (1998).
- [30] M. Garbey, A. Taik, and V. Volpert, *Q. Appl. Math.* **54**, 225 (1996).
- [31] G. Bowden, M. Garbey, V. M. Ilyashenko, J. A. Pojman, S. E. Solovyov, A. Taik, and V. A. Volpert, *J. Phys. Chem. B* **101**, 678 (1997).
- [32] R. Tian, A. De Wit, and L. Rongy, *Adv. Colloid Interface Sci.* **255**, 76 (2018).
- [33] S. Mukherjee and M. Paul, *J. Fluid Mech.* **942** (2022).
- [34] J. A. Pojman, *Math. Model. Nat. Phenom.* **14**, 604 (2019).
- [35] V. Janssens, C. Block, G. Van Assche, B. Van Mele, and P. Van Puyvelde, *Int. Polym. Process.* **25**, 304 (2010).
- [36] E. M. Lloyd, E. C. Feinberg, Y. Gao, S. R. Peterson, B. Soman, J. Hemmer, L. M. Dean, Q. Wu, P. H. Geubelle, N. R. Sottos *et al.*, *ACS Cent. Sci.* **7**, 603 (2021).
- [37] M. Belk, K. G. Kostarev, V. Volpert, and T. M. Yudina, *J. Phys. Chem. B* **107**, 10292 (2003).
- [38] D. G. Ivanoff, J. Sung, S. M. Butikofer, J. S. Moore, and N. R. Sottos, *Macromolecules* **53**, 8360 (2020).
- [39] D. Gaston, C. Newman, G. Hansen, and D. Lebrun-Grandie, *Nucl. Eng. Des.* **239**, 1768 (2009).
- [40] See Supplemental Material at <http://link.aps.org/supplemental/10.1103/PhysRevLett.130.028101> for thermal and cure kinetics parameters of the resin, dynamic viscosity variation during the polymerization, front velocity, effects of glass molds, and experiment methods.

- [41] A. Kumar, Y. Gao, and P. H. Geubelle, *J. Polym. Sci.* **59**, 1109 (2021).
- [42] Y. Gao, M. A. Dearborn, S. Vyas, A. Kumar, J. Hemmer, Z. Wang, Q. Wu, O. Alshangiti, J. S. Moore, A. P. Esser-Kahn *et al.*, *J. Phys. Chem. B* **125**, 7537 (2021).
- [43] E. Goli, T. Gai, and P. Geubelle, *J. Phys. Chem. B* **124**, 6404 (2020).
- [44] Y. Gao, L. E. Rodriguez Koett, J. Hemmer, T. Gai, N. Parikh, N. R. Sottos, and P. H. Geubelle, *ACS Appl. Polym. Mater.* **4**, 4919 (2022).